Energy transport in short-pulse-laser-heated targets measured using extreme ultraviolet laser backlighting

L. A. Wilson,[1,*] G. J. Tallents,[1] J. Pasley,[1] D. S. Whittaker,[1] S. J. Rose,[2] O. Guilbaud,[3] K. Cassou,[3] S. Kazamias,[3] S. Daboussi,[3] M. Pittman,[3] O. Delmas,[3] J. Demailly,[3] O. Neveu,[3] and D. Ros[3]

[1]*York Plasma Institute, The Department of Physics, The University of York, York YO10 5DQ, UK*

[2]*Imperial College London, South Kensington Campus, London SW7 2AZ, UK*

[3]*LASERIX, Université Paris-Sud, Campus de l'ENSTA, Chemin de la Hunière, F-91761 PALAISEAU Cedex, France.*

(Received 13 December 2011; revised manuscript received 26 June 2012; published 28 August 2012)

The accurate characterization of thermal electron transport and the determination of heating by suprathermal electrons in laser driven solid targets are both issues of great importance to the current experiments being performed at the National Ignition Facility, which aims to achieve thermonuclear fusion ignition using lasers. Ionization, induced by electronic heat conduction, can cause the opacity of a material to drop significantly once bound-free photoionization is no longer energetically possible. We show that this drop in opacity enables measurements of the transmission of extreme ultraviolet (EUV) laser pulses at 13.9 nm to act as a signature of the heating of thin (50 nm) iron layers with a 50-nm thick parylene-N (CH) overlay irradiated by 35-fs pulses at irradiance 3×10^{16} Wcm^{-2}. Comparing EUV transmission measurements at different times after irradiation to fluid code simulations shows that the target is instantaneously heated by hot electrons (with approximately 10% of the laser energy), followed by thermal conduction with a flux limiter of $\approx$0.05.

DOI: 10.1103/PhysRevE.86.026406 PACS number(s): 52.57.−z, 42.55.Vc, 52.38.Mf

I. INTRODUCTION

Current inertial confined fusion (ICF) experiments use optical lasers to initiate nuclear fusion in a small fuel pellet with the inertia of the fuel mass providing confinement. The National Ignition Facility (NIF) is utilizing 192 lasers to produce ignition of the fuel using an "indirect" drive [1,2], while other laboratories are pursuing a "direct" drive approach which may be needed for commercial energy production [3]. In direct drive ICF, symmetric laser irradiation of a spherical shell containing deuterium and tritium is engineered so that the ablation of the shell material causes a momentum-conserving implosion of the deuterium and tritium via a series of shock waves. The efficiency of direct drive ICF is highly dependent on the energy flow from the region where the laser energy is deposited, to the ablation surface [4]. In indirect drive ICF, the spherical shell with deuterium and tritium is contained within a "hohlraum" cavity and the cavity walls are heated by lasers to produce x rays which uniformly ablate the shell material to produce an implosion of the deuterium and tritium [5] via a series of coalescing shocks. Understanding the heating of the cavity walls to produce x rays is particularly important towards the end of the laser pulse when a final shock wave is driven to compress the fuel to ignition and a significant buildup of plasma expanding from the hohlraum wall means the laser energy can be absorbed away from the wall.

In experiments where high power optical laser pulses are focused onto a solid target, the laser typically interacts via inverse bremsstrahlung and collective processes with lower density plasma expanding away from the target surface as laser light only penetrates through an expanding plasma plume up to the critical electron density. The critical electron number density n_c has a value $\frac{10^{21}}{\lambda^2}$cm^{-3} where the laser wavelength is measured in microns and is, consequentially, found at a mass density typically a factor 10^{-2}–10^{-3} smaller than the solid density. There are steep density and temperature gradients from the hot (>100 eV) critical density surface to an ablation surface where cooler, denser material is being heated by thermal conduction.

As well as absorption by inverse bremsstrahlung and by collective processes such as resonance absorption [6], additional processes such as stimulated Raman scattering and stimulated Brillouin scattering can occur near the critical density [7]. Absorption was found to vary between $A \approx 40\%$ at long wavelengths increasing to $\approx$80% at shorter wavelengths($\lambda < 1$ μm) at the irradiance and nanosecond pulse lengths of interest for ICF (10^{14}–10^{16} Wcm^{-2}) [3,8]. At shorter femtosecond-picosecond pulse lengths, absorption is typically $A \approx 30\%$. Resonance absorption can be strongly dependant on the angle of incidence of the heating pulse, particularly with short pulse irradiation on a steep density gradient [9,10]. The collective processes (e.g., resonance absorption, stimulated Raman scatter, and stimulated Brillouin scatter) may produce suprathermal electrons with much larger energies than the energies of the surrounding thermal electrons. Such high energy electrons often penetrate into the solid target and heat it before thermal conduction occurs, which is particularly disadvantageous in ICF as the preheated fuel is more difficult to compress.

The thermal flow rate q of energy from the critical density surface to the ablation surface in laser-produced plasmas has been shown to deviate significantly from the classical heat flow rate $q_{SH} = -\kappa \nabla T_e$, where ∇T_e is the electron temperature gradient and κ is the classical plasma thermal conductivity [11]. In fluid code modeling of the steep density and temperature gradient region between the critical and ablation surfaces, it was found that the thermal flow of energy needs to be heuristically adjusted to be less than or equal to a fixed ratio f (known as the "flux limiter") of the much

*law504@york.ac.uk

higher heat flow rate obtained for free-streaming electrons. For electron density n_e and average electron velocities v_e, the free-streaming heat flow rate is $q_{fs} = v_e n_e k T_e$ (where k is Boltzmann's constant). Early empirical comparisons of fluid simulations with experiments indicated $f \approx 0.03$–0.05 [12], while Fokker-Planck modeling of the energy flow for realistic gradients suggested $f \approx 0.1$ [13,14]. Recent work simulating converging shock waves with fluid codes and other experiments relevant to direct drive ICF has revisited the issue of the value of the flux limiter [3,15–17] and the correct value of the flux limiter is an issue in modeling x-ray production from the NIF hohlraum wall in indirect drive [18,19]. The recent integrated experiments at the NIF have made it clear that more extensive benchmarking of the electron transport models employed in the design of ICF targets is necessary to have a satisfactory predictive capability. However, on more complex experiments, such as the implosion and hohlraum energetics experiments being performed at the NIF, it is difficult to resolve the effects of the many different uncertainties that are present. Here, an experimental methodology which enables the effects of electron heat conduction to be measured in a more direct fashion is presented.

In this article, we present measurements of the transmission of an extreme ultraviolet (EUV) laser backlighter of photon energy 89 eV through sample targets with an iron layer (50-nm thick) buried in plastic (50-nm overlay). The 50-nm thick iron layer is highly opaque to the EUV radiation at room temperature (transmission = 0.08), while the plastic overlay is relatively transparent (transmission = 0.85). As energy from the laser is conducted from the lower density absorption region to the high density solid material, the iron layer is heated and ionized. When ionization to Fe^{5+} (ionization energy 99.1 eV) occurs, bound-free absorption in the iron is no longer energetically possible, so the iron becomes highly transparent. We show that this switch in the transparency of the iron acts as a direct signature of the heat penetration into the target and enables a measure of the heat flow into the target.

II. EUV LASERS AND EUV OPACITY

Plasma-based soft x-ray or EUV lasers have produced output in the range 5.9–46.9 nm at well-defined wavelengths with spectral bandwidth $\frac{\lambda}{\Delta\lambda} \approx 10^3$–$10^4$ [20]. Capillary discharge lasers have output up to 1 mJ per pulse in nanosecond duration output [21] at 46.9 nm, while shorter wavelength lasing down to the soft x ray at 5.9 nm has been observed using visible or infrared lasers as a pump [22]. Population inversions are created by electron collisional pumping to metastable states in Ne-like or Ni-like ions leading to lasing between, respectively, $3p$–$3s$ states or $4d$–$4p$ states. The efficiency of the shorter wavelength lasers increases significantly using grazing-incidence pumping as the pumping laser energy is efficiently coupled to the optimum plasma density region for gain [23].

Due to their brightness and monochromaticity, plasma-based EUV lasers have been used as backlighters in laser-plasmas experiments to study the imprinting of the Rayleigh-Taylor instability [24,25], to measure the opacity of high energy density plasma material [26], and to measure the laser ablation rate of a target [27]. Careful design is needed to optimize the targets for each application, but the signature effect on EUV transmission can be large. If EUV interferometry is employed, it has been shown that the refractive index effects associated with photoionization also produce a signature of low level ionization between the critical and ablation surfaces [28]. The signature of a rapid change of opacity with ionization has been used for the measurement of ablation [27] and is employed here to measure heat transport.

Measurements of the EUV absorption of iron plasmas have previously been undertaken using high Z, quasicontinuum spectrally broad backlighters impinging on radiatively heated iron foils. Examples of these types of experiments have been reported by Da Silva *et al.*, Winhart *et al.*, and Springer *et al.* [29–31]. Measurements of iron absorption at densities of ≈ 0.01 gcm^{-3} with measured iron electron temperatures (and photon energies in brackets) of 25 eV (50 eV $\leqslant h\nu \leqslant$ 120 eV), 20 eV (70 eV $\leqslant h\nu \leqslant$ 280 eV), and 59 eV (90 eV $\leqslant h\nu \leqslant$ 300 eV), respectively, have been made. Spectrally broad backlighter measurements are limited at high temperatures and densities as the self-emission from a heated target can overwhelm the backlighter emission.

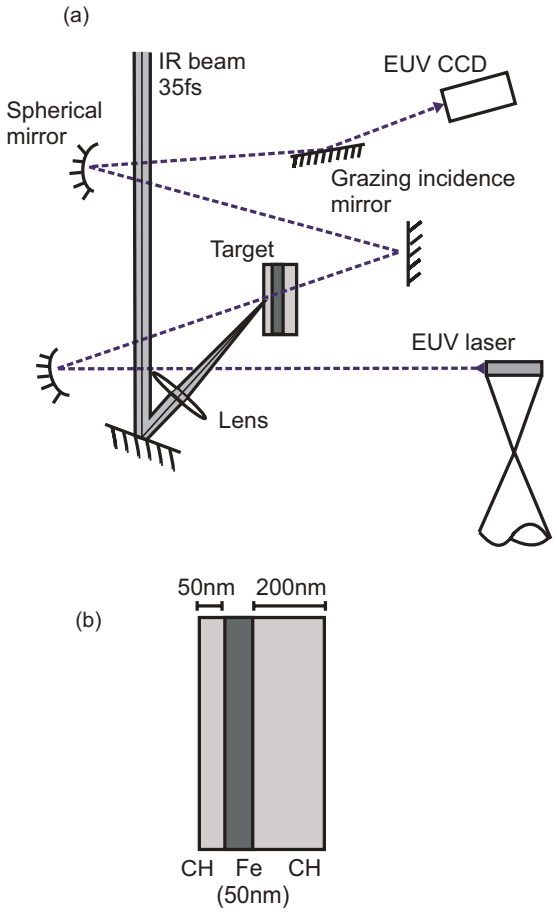

FIG. 1. (Color online) (a) Schematic showing the measurement of EUV laser transmission through a short pulse (35 fs) laser heated iron layer (50 nm) buried in plastic (CH). The EUV laser is focused onto the target and the target EUV transmission is imaged onto a CCD camera. (b) A schematic of the iron buried layer target.

III. EUV TRANSMISSION MEASUREMENTS

For this experiment, EUV radiation of pulse energy ≈1 μJ at wavelength 13.9 nm (photon energy 89 eV) from Ni-like silver laser output was produced at the LASERIX facility [32] using grazing-incidence irradiation of a solid silver slab with 800-nm wavelength laser light comprising a deliberate 500 ps, 400 mJ prepulse and a 4 ps, 1 J main pulse. The EUV laser divergence was measured as 5 mrad × 10 mrad. The EUV laser output was focused onto a sample tamped iron target using a 300-mm focal length spherical multilayer mirror positioned at 7° to the target normal. A diagram of the experimental setup is shown in Fig. 1. The EUV laser flux transmitted through the target was imaged with a magnification of 4 using a 500-mm focal length spherical multilayer mirror onto a CCD detector. A gold coated grazing-incidence mirror (grazing angle 7°) and 0.15-μm thick zirconium filter before the CCD detector were employed to remove, respectively, short wavelength (<8 nm) and long wavelength (>17 nm) emissions from the sample target. The duration of the EUV laser pulse determines the temporal resolution of the measurement and is estimated from experiments and modeling studies to be less than 3 ps [33]. The wavelength of the EUV laser has been accurately measured as 138.92 Å ± 0.15 Å [34].

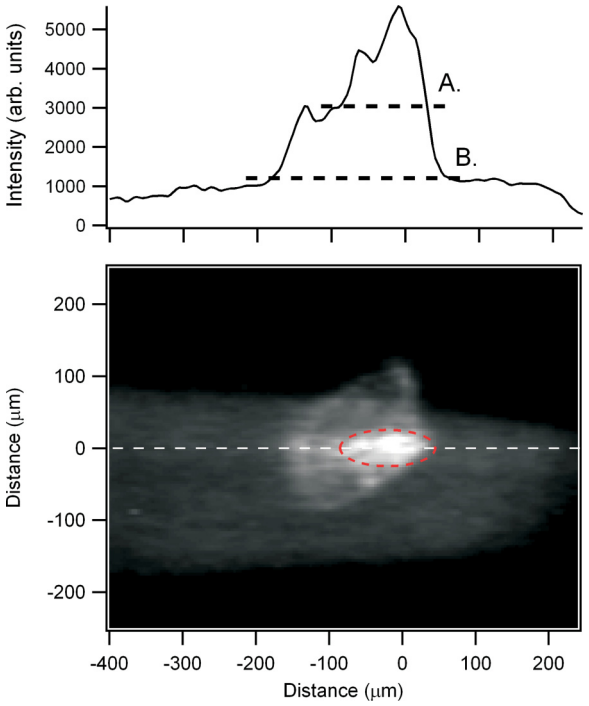

FIG. 2. (Color online) Image of the EUV laser radiation at 89 eV transmitted through a CH tamped 50-nm thick iron target at time 130 ps. The EUV radiation is transmitted through a largely unirradiated portion of the target (over 200 × 150 μm^2) with a smaller section of higher transmission where irradiation with a 35-fs laser pulse has heated the iron (encircled). On the line-out, A represents the level of EUV radiation transmitted through the unheated target, while B represents the base level of background signal found to be associated with self-emission from the tamped iron target. The large, over 600 × 200 μm^2 area of emission is due to scattered self-emission.

The sample targets used for the heat flow study were irradiated by an 800 nm, 35 mJ, *p*-polarized pulse of duration 35 fs incident at 20° to the target normal focused by a 200-mm focal length lens. The sample targets consisted of a flat iron foil of 50-nm thickness tamped on the backside by 200 nm of parylene-N (CH) and on the front-side by 50 nm of parylene-N. Prepulse irradiation commencing 40 ps before the main pulse initially at 10^{-7} contrast ramping to 10^{-4} contrast at 1 ps before the 35 fs pulse was measured using a third-order autocorrelator.

A sample image of the EUV laser transmission through a tamped iron target at time 130 ps after the main pulse recorded on the CCD detector is shown in Fig. 2. Using an EUV laser backlighter source and heavy filtering away from the backlighter laser wavelength has ensured that the transmitted backlighter signal is much brighter than the plasma self-emission. The EUV laser beam transmission through the 800-nm laser irradiated area and the unirradiated area is clearly apparent (Fig. 2). By recording images with and without an incident EUV laser and with and without an iron target heating pulse, it was verified that there is only a spatially broad fluorescence arising from plasma self-emission and that the increase in recorded signal at the focal position (the bright region on Fig. 2) is due to the increased transmission of the EUV laser through the target. The transmission through the target has been measured from plots such as Fig. 2 by comparing the spatially broad EUV laser intensity transmitted where no heating has occurred and the EUV intensity transmitted at the center of the 35-fs laser focal spot. With our procedure we found that the measured cold target EUV transmission is in agreement with tabulated values [35].

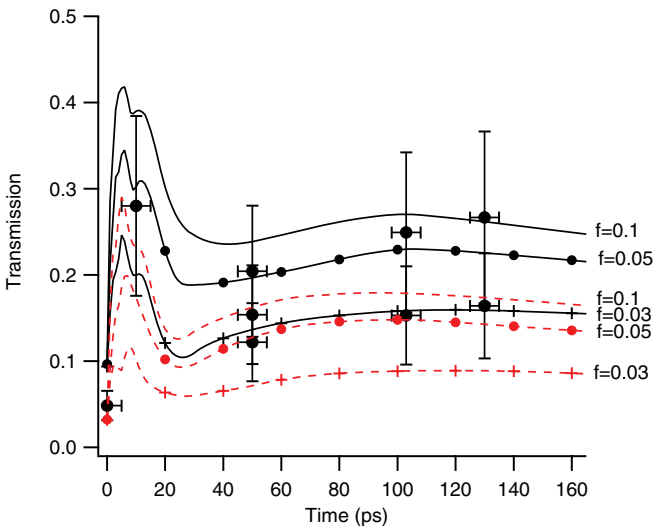

FIG. 3. (Color online) Transmission of EUV laser radiation at 89 eV as a function of time through a tamped 50-nm thick iron target. The target is irradiated at 0 ps by a 3 × 10^{16} Wcm^{-2} peak irradiance pulse of 35-fs duration. Simulation results using the HYADES code and a revised IMP opacity model postprocessor are superimposed on the measured transmissions (shown with error bars). Simulation results are shown for various values of flux limiter (as labeled) calculated assuming (i) energy transport occurs via thermal conduction only (dotted curves) and (ii) hot electrons dump a fraction 10% of the laser pulse energy through the target at 0 ps and then energy transport occurs via thermal conduction (solid curves).

Varying the timing between the EUV laser creation pulses and the sample target heating beam enabled the transmission of the EUV laser at different times in the laser interaction with the tamped iron target to be measured (Fig. 3). The errors in the transmission of the EUV laser are due to the variation of the intensity of the EUV laser over the beam area and the spatial variation of the center of the 35-fs focal spot irradiance. These errors are indicated by the error bars in Fig. 3. The shot to shot variation between the data points is due to variations in irradiance of the heating beam, with each data point representing a single shot. Although the laser system can operate up to 10 Hz, it was necessary to re-position a replacement target for each shot. The Fig. 2 images of the transmitted EUV laser flux enable a measure of the target area irradiated by the 35-fs optical pulse. From Fig. 2 and similar images, the irradiated area is 100 μm $\times$ 50 μm implying peak irradiances of 3×10^{16} Wcm^{-2}. This measurement of the focal spot diameter is in agreement with measurements made by imaging the attenuated laser beam. Some spatial frequency chirp is apparent in the focal spot causing the elliptical focal region (see Fig. 2), but this does not affect the results presented here.

IV. SIMULATIONS OF EUV TRANSMISSION

The one-dimensional radiation hydrodynamics code HYADES [36] was used to simulate the irradiated tamped iron target temperatures, ionization, and density as a function of time and distance from which the EUV transmission was calculated. The code uses the Los Alamos Sesame library [37] for the equation of state of the plasma material. The laser energy deposition in the expanding plasma profile is modeled by calculating the rate of inverse bremsstrahlung and resonance absorption for p-polarized light incident at 20° to the target normal. The measured prepulse irradiation profile with an assumed Gaussian pulse shape of 35-fs full-width half maximum width at the time of the main pulse was used as a temporal profile for the laser irradiation. The effect on the calculated EUV transmission of the presence of a low level prepulse was found to be important, but the exact shape and level of the prepulse (to within a factor of 3 in contrast) was not significant. The effective energy flow rate q between the critical and ablation surfaces was calculated using $\frac{1}{q} = \frac{1}{q_{SH}} + \frac{1}{f q_{fs}}$, where $q_{fs} = \nu_e n_e k T_e$, $q_{SH} = -\kappa \nabla T_e$, and f is the flux limiter.

A postprocessor was used to calculate the transmission T through the target of the 13.9-nm EUV radiation (photon energy 89 eV) from the fluid code calculated electron temperature T_e, mass density ρ, and cell dimensions. The tabulated opacity σ values from the ionized materials package (IMP) code [38,39] which assumes local thermodynamic equilibrium (LTE) ionization balance were employed to give the transmission T using

$$T = \exp\left(-\int \rho\sigma dx\right),$$

where the integration is through the target at the 7° incidence angle to the target normal of the EUV laser beam. The opacities are dominated by the effect of photoionization (bound-free processes) in iron ions with ionization energy less than the photon energy. The opacities become small when ions of charge state Fe^{5+} with ionization energy 99.1 eV (or higher) predominate. Ions of lower ionization (e.g., Fe^{4+} with ionization energy 75.0 eV) heavily absorb the 89 eV photons. The plastic opacity is also modeled in the postprocessor code, but the plastic layers have only a small effect on the overall

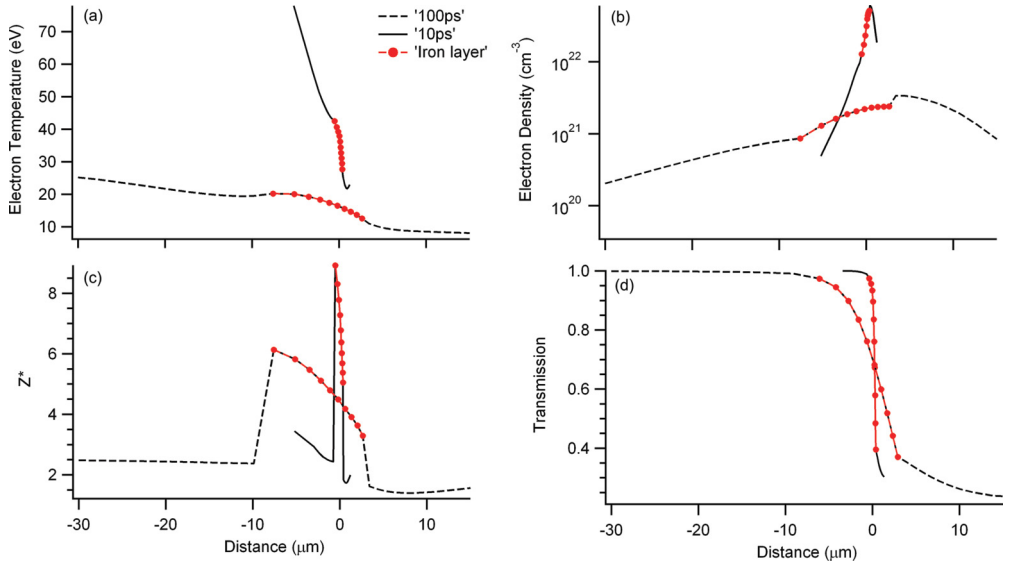

FIG. 4. (Color online) Cross sections of (a) sample electron temperature T_e, (b) electron density n_e, (c) average ionization Z^*, and (d) target transmission T as a function of distance from the target surface at 10 ps (full line) and 100 ps (broken line) after the irradiation of the target as illustrated in Fig. 1(b) with peak irradiance 3×10^{16} Wcm^{-2} in a 35-fs pulse (with prepulse). The results are simulated using the HYADES code with a flux limiter of 0.05 and an assumed dump of 10% of the laser energy into hot electrons which are deposited proportionally to the mass density in the target. The position of the iron component of the target is indicated by superimposed circles. The heating laser pulse is assumed incident from the left (negative distance positions). A prepulse starting 70 ps before the 35-fs pulse as measured in the experiment is assumed for the simulations.

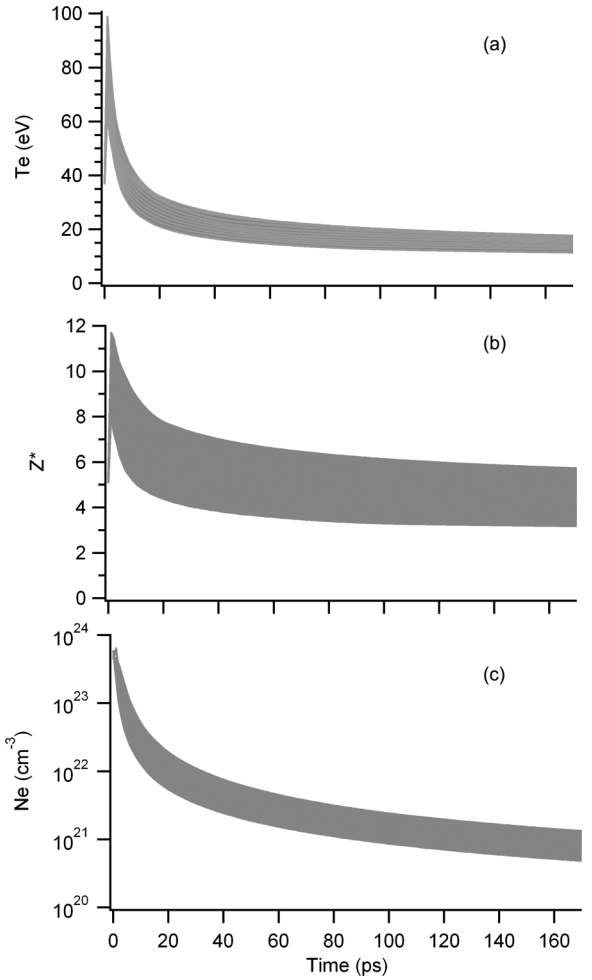

FIG. 5. (a) Sample target electron temperature T_e, (b) average ionization Z^*, and (c) electron density n_e within the iron layer as a function of time from the arrival time of the heating pulse simulated using the HYADES code at a peak intensity of 3×10^{16} Wcm^{-2} calculated with a flux limiter of 0.05 and 10% hot electron energy dump in the target. A prepulse starting at time (70 ps as measured in the experiment followed by the 35-fs pulse at time "0 ps") is assumed for the simulation.

target transmission as the tamped overlay transmission is initially high at 0.85 and with heating only increases closer to 1 (see Fig. 4). Figure 4 shows the electron temperature, electron density, average ionization (Z^*), and transmission throughout the target at times 10 and 100 ps after the 35-fs heating pulse. Figures 4 and 5 show a decrease in spatial variation in the iron layer conditions with time. For example, the variation in electron temperature across the iron layer is 15 eV at 10 ps reducing to 8 eV at 100 ps and 6 eV at 170 ps. A similar trend of increasing uniformity with time is also seen in the electron density and average ionization. Peak values of temperature, ionization, and density occur at time 1 ps. The peak in the EUV transmission of the iron occurs later at 6 ps (see Fig. 3) as the electron density begins to drop, but the ionization of the iron remains high.

Simulated values of transmission T using a revised IMP opacity model are superimposed on the Fig. 3 experimental transmission results with different values of the flux limiter f and assuming either (i) a model of hot suprathermal electron target heating with a dump of 10% of the laser energy distributed through the target proportionally to the density at time 0 ps, or (ii) no hot electron target heating. With the hot electron heating, the simulated transmissions T are in agreement with the measured transmissions with flux limiter $f = 0.05$–0.1. Without hot electron heating, the simulated transmissions with lower flux limiters ($f < 0.1$) do not correctly predict the rapid rise in EUV transmission observed at early times (10 ps), and a value $f \geqslant 0.1$ best fits the late-time transmissions. With or without hot electron heating, the HYADES code predicts an absorption fraction $A \approx 30\%$ due to inverse bremsstrahlung and resonance absorption, in agreement with measurements and other simulations at the same irradiance [8]. Hot electron target heating with 5–10% of the laser energy has been observed previously for similar irradiation conditions [40,41]. The HYADES simulations show that the iron layer in the target for the times (<130 ps) where transmission is measured (Fig. 3) has densities greater than 10^{-2} gcm^{-3} and so the iron ionization balance is consequently in LTE and so the use of an opacity model (IMP) assuming LTE is valid. An LTE average atom model of ionization was also used in the HYADES simulations.

V. OPACITY DATA COMPARISONS

Two sets of IMP iron opacity data have been compared. The original IMP [38] data used ion configurations based on placing quantum shells in one of three groups. Core shells are assumed to be fully occupied. Rydberg shells are assumed to be empty with one valence shell, which has a varying level of occupation. A more recent set of IMP data has several improvements [39] including a greater number of possible atomic configurations which can contribute significantly to the opacity. The improved IMP data allow for ion configurations with up to three open valence shells with significant populations.

The revised IMP opacity data were found to give better agreement with our measured EUV transmissions. The

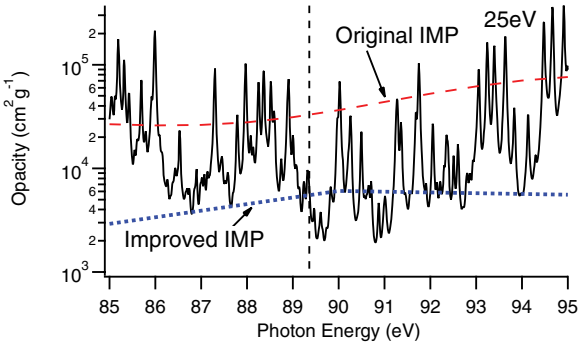

FIG. 6. (Color online) Comparison of different opacity models of iron in the 85–95 eV photon energy region at a density of 0.008 gcm^{-3} and a temperature of 25 eV. The solid line is a detailed line accounting the prediction from the York opacity model [43] using atomic data from the Opacity Project [42]. Data from the IMP opacity model [38] which is accurate for spectrally broad backlighter calculations is also shown (dotted line revised IMP data, dashed line original IMP data). The vertical line shows the photon energy of the EUV laser.

explanation for this can be seen in Fig. 6 which compares both sets of IMP opacity data with frequency-dependent opacities calculated from the Opacity Project atomic data [42,43]. Modeling accurate plasma opacities, in particular for medium to high Z materials, where there are a large number of possible bound-bound transitions over a range of ionization states, is complex and computationally expensive. Code efficiency approximations such as the IMP opacities are required which reduce spectral detail as most opacity applications are used for spectrally broad radiation spectra and not the extreme narrow-band emission ($\frac{\lambda}{\Delta\lambda} \approx 10^3$–$10^4$) from the EUV laser. From Fig. 6, we see that the EUV laser with its characteristic narrow spectral width is positioned between iron absorption lines giving a lower opacity largely unaffected by bound-bound transitions. Using Fig. 6, our EUV transmission measurements also imply that the accuracy of the iron absorption line photon energies calculated by the Opacity Project is <0.4 eV (0.5%) in this photon energy region, as the EUV laser photon energy is known to <0.1 eV accuracy [34]. The accuracies of Opacity Project line wavelengths have previously been estimated to be 1–4% [44].

VI. CONCLUSION

We have shown that a rapid drop in opacity of iron with ionization enables measurements of the transmission of EUV laser pulses at 13.9 nm to act as a signature of the heating of thin (50 nm) iron layers with 50-nm thick parylene-N (CH) overlay irradiated by 35-fs pulses at irradiance $\approx 3 \times 10^{16}$ Wcm^{-2}. Comparing EUV transmission measurements at different times after irradiation to fluid code simulations shows that the target is instantaneously heated by hot electrons with approximately 10% of the laser energy, followed by thermal conduction with a flux limiter of ≈ 0.05. The extent of hot electron target heating and the value of the flux limiter are both critical issues for inertial fusion research. We believe there is scope for further work using this method, with potential for improvements to errors in measurements of transmission possible with improvements to beam uniformity. Data such as obtained in this work are critical for the development of a predictive simulation capability that will render the development of successful inertial fusion experiments possible without substantial empirical design iteration on large facilities, which is both time consuming and costly.

ACKNOWLEDGMENTS

We acknowledge the United Kingdom Engineering and Physical Sciences Research Council (Grant No. EP/F019289/1), European Union LASERLAB2 SFINX (Grant No. 228334), and the Agence Nationale de la Recherche (Grant No. ASOURIX ANR-09-JCJC-0056) support for this work. We thank Dr. James Gaffney for help in providing IMP opacity data.

[1] D. Clery, Science **334**, 449 (2011).
[2] S. Glenzer, B. J. MacGowan, N. B. Meezan, P. A. Adams, J. B. Alfonso, E. T. Alger, Z. Alherz, L. F. Alvarez, S. S. Alvarez, P. Amick *et al.*, Phys. Rev. Lett. **106**, 085004 (2011).
[3] S. P. Regan, R. Epstein, V. N. Goncharov, I. V. Igumenshchev, D. Li, H. S. P. B. Radha, W. Seka, T. R. Boehly, J. A. Delettrez, O. V. Gotchev *et al.*, Phys. Plasmas **14**, 056305 (2007).
[4] S. Atzeni and J. Meyer-ter Vehn, *The Physics of Inertial Fusion* (Oxford Science, Oxford, 1998).
[5] J. Lindl, Phys. Plasmas **2**, 3933 (1995).
[6] W. L. Kruer, *The Physics of Laser Plasma Interactions* (Westview, Boulder, CO, 2003).
[7] C. J. Walsh, D. M. Villeneuve, and H. A. Baldis, Phys. Rev. Lett. **53**, 1445 (1984).
[8] C. Garban-Labaune, E. Fabre, C. E. Max, R. Fabbro, F. Amiranoff, J. Virmont, M. Weinfeld, and A. Michard, Phys. Rev. Lett. **48**, 1018 (1982).
[9] D. C. Slater, G. E. Busch, G. Charatis, R. R. Johnson, F. J. Mayer, R. J. Schroeder, J. D. Simpson, D. Sullivan, J. A. Tarvin, and C. E. Thomas, Phys. Rev. Lett. **46**, 1199 (1981).
[10] P. Gibbon and A. R. Bell, Phys. Rev. Lett. **68**, 1535 (1992).
[11] L. Spitzer and R. Harm, Phys. Rev. **89**, 977 (1953).
[12] R. C. Malone, R. L. McCrory, and R. L. Morse, Phys. Rev. Lett. **34**, 721 (1975).
[13] A. R. Bell, R. G. Evans, and D. J. Nicholas, Phys. Rev. Lett. **46**, 243 (1981).
[14] G. J. Rickard, A. R. Bell, and E. M. Epperlein, Phys. Rev. Lett. **62**, 2687 (1989).
[15] W. Seka, D. H. Edgell, J. F. Myatt, A. V. Maximov, R. W. Short, V. N. Goncharov, and H. A. Baldis, Phys. Plasmas **16**, 052701 (2009).
[16] T. R. Boehly, V. N. Goncharov, W. Seka, S. X. Hu, J. A. Marozas, D. D. Meyerhofer, P. M. Celliers, D. G. Hicks, M. A. Barrios, D. Fratanduono *et al.*, Phys. Plasmas **18**, 092706 (2011).
[17] A. Sunahara, J. A. Delettrez, C. Stoeckl, R. W. Short, and S. Skupsky, Phys. Rev. Lett. **91**, 095003 (2003).
[18] R. E. Olson, L. J. Suter, J. L. Kline, D. A. Callahan, M. D. Rosen, K. Widmann, E. A. Williams, D. E. Hinkel, N. B. Meezan, G. A. Rochau *et al.*, J. Phys: Conf. Ser. **244**, 032057 (2010).
[19] M. Rosen, H. Scott, D. Hinkel, E. Williams, D. Callahan, R. Town, L. Divol, P. Michel, W. Kruer, L. Suter *et al.*, High Energy Density Physics **7**, 180 (2011).
[20] G. J. Tallents, J. Phys. D: Appl. Phys. **36**, R259 (2003).
[21] C. D. Macchietto, B. R. Benware, and J. J. Rocca, Opt. Lett. **24**, 1115 (1999).
[22] R. Smith, G. J. Tallents, J. Zhang, G. Eker, S. McCabe, G. J. Pert, and E. Wolfrum, Phys. Rev. A **59**, R47 (1999).
[23] N. Booth, M. H. Edwards, Z. Zhai, G. J. Tallents, T. Dzelzainis, C. L. S. Lewis, A. Behjat, Q. Dong, S. J. Wang, D. Neely *et al.*, Euro. Phys. J. Special Topics **175**, 153 (2009).
[24] D. H. Kalantar, M. H. Key, L. B. DaSilva., S. G. Glendinning, J. P. Knauer, B. A. Remington, F. Weber, and S. V. Weber, Phys. Rev. Lett. **76**, 3574 (1996).

[25] E. Wolfrum, J. Wark, J. Zhang, D. Kalantar, M. H. Key, B. A. Remington, S. V. Weber, D. Neely, S. Rose, J. Warwick *et al.*, Phys. Plasmas **5**, 227 (1998).

[26] M. H. Edwards, D. Whittaker, P. Mistry, N. Booth, G. J. Pert, G. J. Tallents, B. Rus, T. Mocek, M. Koslová, C. McKenna *et al.*, Phys. Rev. Lett. **97**, 035001 (2006).

[27] M. H. Edwards, D. S. Whittaker, G. J. Tallents, P. Mistry, G. J. Pert, B. Rus, T. Mocek, M. Kozlová, J. Polan, A. Praeg *et al.*, Phys. Rev. Lett. **99**, 195002 (2007).

[28] L. M. R. Gartside, G. J. Tallents, A. K. Rossall, E. Wagenaars, D. S. Whittaker, M. Kozlova, J. Nejdl, M. Sawicka, J. Polan, M. Kalal *et al.*, Opt. Lett. **35**, 3820 (2010).

[29] L. B. Da Silva, B. J. MacGowan, D. R. Kania, B. A. Hammel, C. A. Back, E. Hsieh, R. Doyas, C. A. Iglesias, F. J. Rogers, and R. W. Lee, Phys. Rev. Lett. **69**, 438 (1992).

[30] G. Winhart, K. Eidmann, C. Iglesias, A. Bar-Shalom, E. Mínguez, A. Rickert, and S. Rose, JQSRT **54**, 437 (1995).

[31] P. T. Springer, D. J. Fields, B. G. Wilson, J. K. Nash, W. H. Goldstein, C. A. Iglesias, F. J. Rogers, J. K. Swenson, M. H. Chen, A. Bar-Shalom *et al.*, Phys. Rev. Lett. **69**, 3735 (1992).

[32] D. Ros *et al.*, *X-ray lasers 2010: Proceedings of the 12th International Conference on x-ray lasers, 30 May-4 June 2010, Gwangju, Korea*, edited by J. lee, C. H. Nam, K. A. Janulewicz, Vol. 136 (Springer, Dordrecht, 2011), p. 32.

[33] P. Mistry, G. J. Tallents, and M. H. Edwards, Phys. Rev. A **75**, 013818 (2007).

[34] Y. Li, J. Nilsen, J. Dunn, A. L. Osterheld, A. Ryabtsev, and S. Churilov, Phys. Rev. A **58**, R2668 (1998).

[35] Center for X-ray Optics Lawrence Berkeley National Laboratory, http://henke.lbl.gov/optical_constants.

[36] J. T. Larsen and S. M. Lane, JQSRT **51**, 179 (1994), code commercially available from Cascade Applied Sciences Inc., Larsen@casinc.com.

[37] S. P. Lyon and J. D. Johnson, Los Alamos National Laboratory Report No. LA-UR-92-3407 (1992).

[38] S. J. Rose, J. Phys. B **25**, 1667 (1992).

[39] J. A. Gaffney and S. J. Rose, High Energy Density Physics **5**, 216 (2009).

[40] G. J. Tallents, M. H. Key, P. Norreys, D. Brown, J. Dunn, and H. Baldis, Phys. Rev. A **40**, 2857 (1989).

[41] H. Chen, B. Soom, B. Yaakobi, S. Uchida, and D. D. Meyerhofer, Phys. Rev. Lett. **70**, 3431 (1993).

[42] M. J. Seaton, Y. Yan, D. Mihalas, and A. K. Pradhan, MNRAS **266**, 805 (1994).

[43] D. S. Whittaker and G. J. Tallents, MNRAS **400**, 1808 (2009).

[44] D. J. Heading, J. S. Wark, R. W. Lee, R. Stamm, and B. Talin, Phys. Rev. E **56**, 936 (1997).